Contents lists available at ScienceDirect

Journal of Volcanology and Geothermal Research

Origin of Holocene trachyte lavas of the Quetrupillán volcanic complex, Chile: Examples of residual melts in a rejuvenated crystalline mush reservoir

Raimundo Brahm [a,e,*], Miguel Angel Parada [a,e], Eduardo Morgado [a,b,e], Claudio Contreras [a,c,e], Lucy Emma McGee [a,d,e]

[a] Department of Geology, Universidad de Chile, Santiago, Chile
[b] Institute of Geophysics and Tectonics, School of Earth and Environment, University of Leeds, Leeds LS2 9JT, UK
[c] School of Earth Sciences, University of Bristol, Bristol BS8 1RJ, UK
[d] Department of Earth and Planetary Sciences, Macquarie University, Sydney, Australia
[e] Centro de Excelencia en Geotermia de los Andes (CEGA), Santiago, Chile

ARTICLE INFO

ABSTRACT

The Quetrupillán Volcanic Complex (QVC) is a stratovolcano placed in the center of a NW-SE volcanic chain, between Villarrica volcano and Lanín volcano, in the Central Southern Volcanic Zone of the Andes. Its youngest effusive products are dominated by crystal-poor (most samples with <9 vol% phenocrysts), crystal clot-bearing trachytes (from 64.6 up to 66.2 wt% SiO_2), whereas the oldest units are mainly basaltic andesites. Two-stage generation of QVC trachytes by differentiation at shallow depth (<1 kbar) and NNO-QFM oxidation conditions were obtained from initial melt compositions equivalent to the Huililco basalts, a small eruptive centre located ca. 12 km NE of the QVC main vent. Pyroxene-bearing crystal clots, locally abundant in the trachytes, were formed at 900–960 °C ($\pm$55 °C) and represent a dismembered crystal mush from which interstitial trachytic melts were extracted and transported upward before eruption. Heating of the crystal mush by a hotter magma recharge is inferred from complex zoned plagioclases formed at higher crystallization temperatures (50–90 °C) than those obtained from pyroxene. Ca-rich plagioclase overgrowths around more albitic cores, followed by an external rim of similar composition to the core are interpreted as restoration to the initial conditions of plagioclase crystallization after the mentioned heating event. Additionally, a late heating of up to 150 °C just prior to eruption is recorded by Fe-Ti oxide thermometry.

© 2018 Elsevier B.V. All rights reserved.

1. Introduction

At shallow levels of the crust, magma is commonly stored as highly crystalline (>50 vol% crystals) mushy chambers, where melt extraction from the crystal network is allowed by the hampering of convection, inducing the accumulation in the upper parts of the chamber of more differentiated crystal-poor eruptible magma (Bachmann and Bergantz, 2004; Hildreth, 2004). The survival of highly crystalline silicic reservoirs in the crust is aided by the thermal isolation effect of the crystal network (Ellis et al., 2014) and the relevant amount of latent heat released during crystallization, giving rise to a somewhat steady state in the magma evolution (Huber et al., 2009). In fact, the highly crystalline magmatic chambers can behave like rheological barriers to the intrusion of a

new magma batch (Kent et al., 2010), inhibiting mixing and forcing this batch to stall beneath the bottom of the chamber, unless the intrusion rate is high enough, to produce mush rejuvenation and magma remobilization by dikes (Wright et al., 2011). The remobilization of the trapped melts often produces the crystal clots and antecrysts to be dragged upward from the mush and transported to the melt accumulation zone (Huber et al., 2011). These crystal phases could record magma recharge processes such as thermal and compositional mixing by changes in their chemical composition and evidences of disequilibrium textures (Davidson et al., 2007; Millet et al., 2014). For example, zoning patterns in plagioclase are widely used to track changes in magma conditions (Berlo et al., 2007; Cashman and Blundy, 2013; Streck et al., 2008; among others) because they are commonly present during the whole differentiation process, have slow diffusion rate of mayor elements (Grove et al., 1984; Liu and Yund, 1992) and record compositional changes that depends on of multiple variables (e.g. melt composition, temperature, pressure and H_2O content; Lange et al., 2009; Almeev et al., 2012; Waters and Lange, 2015). We studied

Holocene trachyte lavas of the Quetrupillán Volcanic Complex (QVC), a very uncommon composition in the Andean Southern Volcanic Zone by combining whole-rock compositions, mineral chemistry and simulations to understand the magma differentiation processes that gave rise to the trachytes and determine their pre-eruptive conditions. The studied trachytes are crystal-poor lavas with locally abundant crystal clots, which could be testimonies of a disrupted crystal network (mush zone). We find that the mush zone experienced at least two pre-eruptive events of rejuvenation by interaction (chemical and/or thermal) with hot mafic magma at shallow levels of the crust (<1 kbar), recorded as complex zonation patterns in plagioclase phenocrysts and as conflicting temperature estimates calculated with thermometry methods of slow- and fast-equilibrated mineral phases.

2. Geological background

The current QVC is located to the East of the Liquiñe-Ofqui Fault Zone, a major intra-arc structure of the Andean Southern Volcanic Zone, and forms part of the NW-SE volcanic chain (~39°30′S; constituted by the Villarrica, Quetrupillán and Lanín volcanoes; Fig. 1a). The basement of the QVC is composed of Cretaceous and Miocene plutons and Paleocene to Pliocene stratified volcanoclastic units (Lara and Moreno, 2004; Moreno and Lara, 2008).

The QVC is built above an 8 km-diameter collapse caldera and its summit (2360 m.a.s.l.) was truncated by a later explosive event during pre- to intra-glacial stages. The last eruption of the QVC was registered on July 06, 1872 (Petit-Breuilh, 1994). There are no extensive studies about the QVC history, but preliminary studies of Pavez (1997) defined four units dominated by bimodal products of mainly andesitic and dacitic compositions. The youngest unit is constituted by postglacial materials composed of pyroclastic deposits and blocky trachytic lava flows. The lava flows were sourced from the eleven parasitic centres that surround the southern flank of the main edifice (Fig. 1b). One voluminous lava flow erupted from the main vent and was deposited over

the northern flank of the main volcanic edifice. Previous geochemical analysis shows that the more evolved compositions concentrate in the later stages of the volcano evolution (Hickey-Vargas et al., 1989).

Because of its proximity to the QVC, Huililco Volcano, a small eruptive centre located ca. 12 km NE of the QVC main vent, is also included in this study. It consists of a scoria cone with two vents and aa lava flows. Three lobes are emplaced to the W, and one to the E. These lava flows are emplaced over preglacial volcanic products of the QVC.

3. Sampling and analytical methods

Twelve trachyte samples were collected from blocky lava flows and bombs of eight Holocene parasitic centres located in the southern flank of the QVC (AC1 to AC8; Fig. 1b). Eight trachyte samples were also collected from the Holocene blocky lava flows emitted from the main vent toward the north flank of the volcano (MV; MV1 to MV8). Additionally, a pre-Holocene aa lava emitted from the main QVC vent was also collected (PG1; Fig. 1b). This lava was affected by strong glacial erosion and forms part of the basement of the Huililco lava flows. We obtained whole rock analyses of all the collected QVC samples. Whole rock data of Huililco tephra and lava samples are from McGee et al. (2017). Six of the Holocene QVC trachyte samples were also analyzed for isotopic composition and eight trachyte samples were selected for SEM and EPMA analyses. Whole rock compositions were analyzed by Fusion ICP (for major elements), ICP-MS (for trace elements) and FeO contents were obtained through titration at ACT-Labs (Canada). Several international standards were analyzed at the same time to assess data quality. Major element errors on standards were almost all <5%, with the exception of elements such as MnO and P_2O_5 in standard materials which have very low abundances of these elements (see Supplementary material for full error statistics). Accuracy on W-2 and BIR-1a standards was better than 10% for most trace elements, with the exception of Y, which consistently had an error of >15%, and elements of very low abundance or close to detection limit. Detection limits for all elements analyzed are listed in Table 1 and
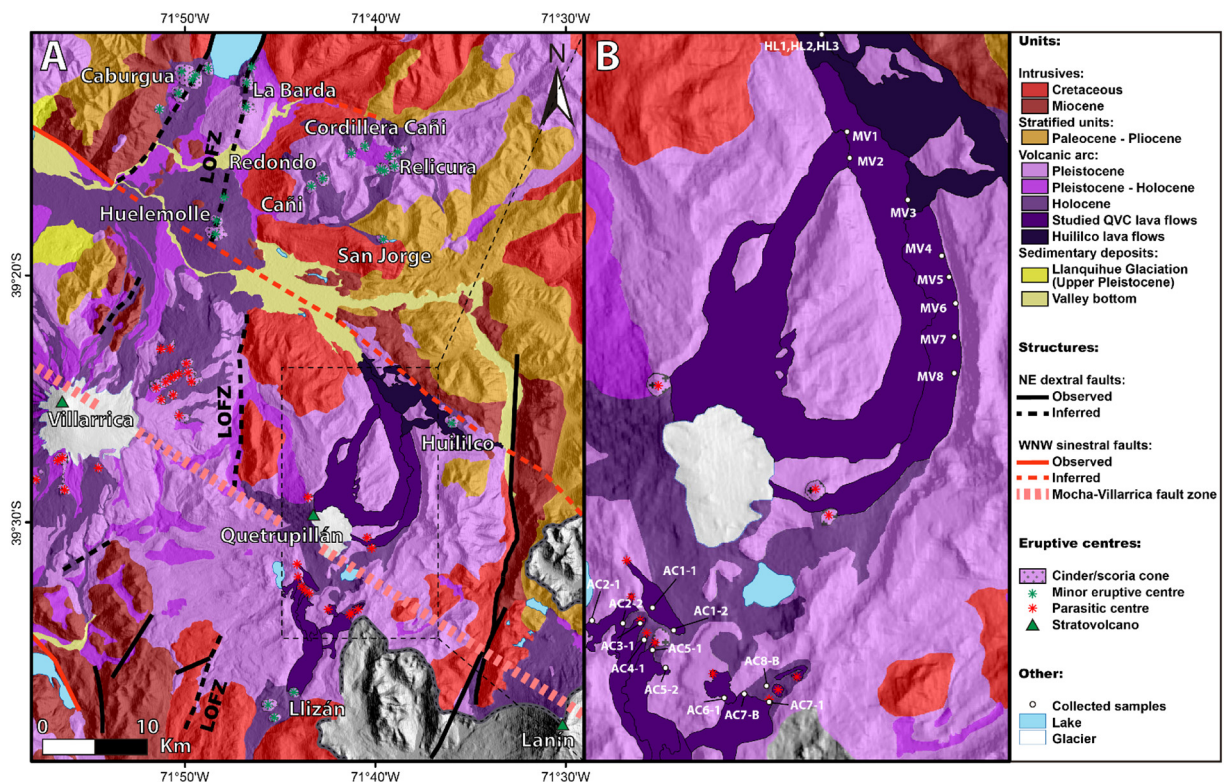

Fig. 1. (A) Simplified geologic map modified from Lara and Moreno (2004) and Moreno and Lara (2008) of the Villarrica-Quetrupillán-Lanín volcanic chain. Structures are after a compilation in Sánchez et al. (2013). LOFZ = Liquiñe-Ofqui Fault Zone. (B) Close-up of the QVC and the studied lava flows, indicating the sampling sites.

can also be found in the Supplementary material. $^{87}Sr/^{86}Sr$ and $^{143}Nd/^{144}Nd$ isotope ratios were obtained with Triton Multi-collector Mass-spectrometer at ACT-Labs using NBS 987 and JNd-1 standards. Uncertainties of $^{87}Sr/^{86}Sr$ estimates reach ±0.000004, whereas the highest uncertainty of $^{143}Nd/^{144}Nd$ estimates is ±0.000019.

Textural recognition and backscatter electron (BSE) images were performed with scanning electron microscopy (FEI Quanta 250) at the University of Chile, where greyscale intensity profiles were measured in plagioclases using backscatter images in JMicrovision software and calibrated with the composition traverses measured by the electron microprobe (eg. Martin et al., 2008; Morgan et al., 2006).

Compositional analyses of mineral phases were performed on the JEOL JXA-8230 electron microprobe at LAMARX – National University of Córdoba. Compositions of all minerals, except plagioclase, were analyzed using a focused beam through single-point measurements in the

core of each phase with an accelerating potential of 15 keV and electron beam current of 20 nA. Plagioclase compositional profiles (spacing mostly between ~10–80 μm; some cases up to 250 μm) were obtained with an accelerating potential of 15 keV and electron beam current of 10 nA with a defocused beam (~5 μm) in order to avoid alkali loss. Counting times for all the phases measured were 10 s on peak and 10 s off peak (5 s at each background position) for major and minor elements. Detection limits of the electron microprobe analyses are listed in Table 2. For more detailed information on the data uncertainties see the Supplementary material.

4. Petrography

All the Holocene QVC trachyte samples are glomeroporphyritic lavas with abundant glass-rich groundmass (Fig. 2a and b). Trachyte samples from the parasitic centres have ca. 6–9 vol% phenocrysts, while those from the main vent show slightly higher phenocryst contents (ca. 11–14 vol%). Phenocrysts occur as isolated crystals (ca. 18–47 vol% of phenocrysts) or forming crystal clots (ca. 53–82 vol% of phenocrysts) and consist of plagioclase (ca. 69–80 vol% of phenocrysts), clino- and orthopyroxene (ca. 10–21 vol% of phenocrysts), Ti-magnetite (titanomagnetite) and ilmenite (ca. 5–13 vol%) and apatite (<5 vol%) (Fig. 2). Trachytes include plagioclase crystals of up to 3.4 mm long and are the biggest crystals usually included in crystal clots. Pyroxene phenocrysts are between >0.1 and 2.9 mm in size, with clinopyroxenes more abundant and larger than orthopyroxene. Fe-Ti oxides occur as small (<0.7 mm in size) crystals, Ti-magnetite being more abundant than ilmenite. Rounded and small pyrrhotite inclusions (≪1 vol%) are common in plagioclase, pyroxene and Fe-Ti oxide phenocrysts. The groundmass is hyalopilitic (ca. 50–70 vol% glass) and contains microlites of plagioclase, pyroxene and Ti-magnetite, in order of increasing abundance. Most phenocrysts and crystal clots are well-preserved, but some crystal clots present pervasive resorption textures with glassy veins (Fig. 2b). Most of the samples are vesiculated (up to 50 vol% vesicles).

The preglacial sample of the QVC (PG1) is petrographically distinct from the main Holocene QVC units. This sample is a nearly aphyric basaltic andesite with scarce (<1 vol%) olivine and plagioclase phenocrysts. Huililco samples are porphyritic (ca. 24 vol% phenocrysts) with phenocrysts of plagioclase (ca. 16 vol%), olivine (ca. 6 vol%) and clinopyroxene (ca. 2 vol%), within an intergranular groundmass with the same minerals. Huililco pyroxenes and plagioclases phenocrysts are found in crystal clots and some plagioclase crystals have strong disequilibrium features such as sieve textures and patchy zones.

5. Whole-rock compositions and isotopic data

Representative whole rock compositions of AC and MV samples can be found in Table 1. All whole rock compositions are presented in the Supplementary material. Taking the available major element compositions of QVC and neighboring volcanoes (Villarrica, Huililco and Lanín), it is possible to observe sub-alkaline affinities and similar compositional gaps (Fig. 3) giving rise to trimodal compositions in terms of SiO_2 content (Hickey-Vargas et al., 1989; Lara, 1997; Lohmar, 2008; McGee et al., 2017; Morgado et al., 2015). The Harker diagrams show that QVC basaltic andesites have constant silica content (from 56.1 wt% up to 56.6 wt%), with a wider dispersion of Al_2O_3 and Fe_2O_3t (~1.5 wt%). QVC trachytes are clustered in small compositional range for most elements (from 64.2 wt% up to 65.8 wt% SiO_2), with the exception of a sample with 62.5 wt% SiO_2. A feature of the QVC trachytes that stands out is the clear decreasing trend of Al_2O_3 with increasing SiO_2 content. Huililco samples are clustered in two groups according their SiO_2 content, basalts ranging from 51.3 wt% up to 52.2 wt% SiO_2 and basaltic andesites between 52.8 wt% and 54.0 wt% SiO_2, but the MgO concentrations of both groups overlap. All samples present the typical Nb-Ta negative anomaly (Fig. 4a) of calc-alkaline magmas in a subduction setting. QVC, Huililco and Lanín products have similar La_N/Yb_N values (5.04 to 6.72), with slightly lower values for the

Table 1
Representative whole rock data from samples of the QVC. Sample LEM-8A from Huililco Volcano (McGee et al., 2017) is also included. AC3-1 = samples from a QVC parasitic centre lava flow. MV4 = sample from QVC main vent lava flow. d.l. = detection limit. The detailed whole data set and associated errors can be found in the Supplementary material.

Mayor elements	d.l. (wt%)	QVC Holocene		QVC Preglacial	Huililco
		AC3-1	MV4	PG1	LEM-8A
SiO_2	0.1	64.09	64.75	55.65	52.3
Al_2O_3	0.01	15.01	15.46	15.4	17.66
TiO_2	0.001	1.118	1.110	1.499	1.083
FeO	0.01	4.2	3.8	–	–
Fe_2O_3	0.01	0.98	1.57	10.84*	9.53*
MnO	0.001	0.128	0.126	0.172	0.153
MgO	0.01	1.24	1.3	2.99	6.24
CaO	0.01	3.33	3.52	6.49	9.16
Na_2O	0.01	4.93	4.91	4.1	3.22
K_2O	0.01	3.00	3.00	1.59	1.08
P_2O_5	0.01	0.36	0.34	0.41	0.34
LOI		−0.21	−0.15	0.31	−0.11
Total		98.17	99.74	99.46	100.7

*Iron content as total Fe_2O_3.

Trace elements	d.l. (ppm)	QVC Holocene		QVC Preglacial	Huililco
		AC3-1	MV4	PG1	LEM-8A
Sc	1	16	15	29	27
V	5	77	82	323	231
Co	1	28	22	22	30
Ga	1	19	20	20	19
Rb	2	79	85	33	26
Sr	2	305	304	431	556
Y	2	38	38	30	20
Zr	4	321	334	178	123
Nb	1	13	12	6	6
Cs	0.5	4	4	1.4	1.2
Ba	3	763	765	514	344
La	0.1	35.8	35.1	23.7	17.8
Ce	0.1	74.5	73.2	51.1	38.8
Pr	0.05	9.47	9.30	6.6	4.88
Nd	0.1	37.4	36.5	28.6	20.1
Sm	0.1	7.7	7.6	6	4.7
Eu	0.05	1.83	1.76	1.69	1.35
Gd	0.1	6.8	6.7	6	4.3
Tb	0.1	1.2	1.1	0.9	0.7
Dy	0.1	6.9	6.8	5.6	3.8
Ho	0.1	1.4	1.4	1.1	0.8
Er	0.1	4.2	4.1	3.6	2.4
Tm	0.05	0.66	0.65	0.55	0.34
Yb	0.1	4.3	4.2	3.5	2.2
Lu	0.04	0.65	0.65	0.51	0.34
Hf	0.2	7.2	7.3	5	3.1
Ta	0.1	0.7	0.7	0.4	0.4
Pb	5	20	20	13	8
Th	0.1	9.7	9.8	5.4	3.3
U	0.1	2.9	2.9	1.6	1
$^{87}Sr/^{86}Sr$		0.704001 ± 4	0.703989 ± 3		
$^{143}Nd/^{144}Nd$		0.512813 ± 10	0.512854 ± 4		

Table 2

Representative compositional analyses of minerals from QVC trachytes. Plg1 and Plg2 are Group 1 and Group 2 plagioclase phenocrysts, respectively. SD = standard deviation (wt%), d.l. = detection limit.

	Plagioclases											
Point	MV7-pl77		MV7-pl90		MV3-pl5		MV3-pl17		AC3-pl161		MV3-pl32	
Type	Plg1				Plg2 core		Plg2 rim		Microlite			
	d.l. (wt%)	wt%	SD	wt%	SD	wt%	SD	wt%	SD	wt%	SD	wt%	SD
SiO_2	0.04	55.54	0.14	58.14	0.15	46.77	0.13	56.84	0.14	56.12	0.14	62.51	0.15
TiO_2	0.03	0.06	0.02	0.03	0.02	–	–	0.07	0.02	0.04	0.02	0.14	0.02
Al_2O_3	0.02	28.68	0.10	26.28	0.09	34.43	0.11	27.82	0.10	27.61	0.10	23.24	0.09
FeO	0.02	0.56	0.03	0.58	0.03	0.52	0.03	0.61	0.03	0.63	0.03	0.58	0.03
MgO	0.02	0.08	0.01	0.01	0.01	0.02	0.01	0.09	0.01	0.06	0.01	0.02	0.01
CaO	0.02	10.19	0.07	7.76	0.06	16.76	0.09	9.48	0.07	9.19	0.07	4.35	0.03
Na_2O	0.01	5.42	0.06	6.51	0.07	1.82	0.04	5.89	0.06	6.17	0.06	8.06	0.07
K_2O	0.01	0.39	0.02	0.50	0.02	0.08	0.02	0.33	0.02	0.34	0.02	1.54	0.02
SrO	0.030	0.182	0.039	0.033	0.035	0.109	0.037	0.124	0.038	0.074	0.038	0.066	0.036
Total		101.09	0.49	99.84	0.48	100.52	0.46	101.24	0.49	100.23	0.49	100.49	0.46
XAn		50		39		83		46		44		21	
XAb		48		58		16		52		54		70	
XOr		2		3		1		2		2		9	

	Clinopyroxene						Orthopyroxene					
Point	AC6-1-px85		AC3-1-px3		MV-3-px173		AC6-1-px86		AC3-1-px4		AC3-1-px22	
Type	Crystal clot		Isolated		Microlite		Crystal clot		Isolated		Microlite	
	d.l. (wt%)	wt%	SD	wt%	SD	wt%	SD	wt%	SD	wt%	SD	wt%	SD
SiO_2	0.03	52.06	0.09	51.20	0.09	51.33	0.09	53.53	0.10	53.74	0.10	53.81	0.10
TiO_2	0.02	0.64	0.02	0.87	0.02	0.92	0.02	0.29	0.02	0.33	0.02	0.33	0.02
Al_2O_3	0.01	1.49	0.02	2.14	0.02	2.54	0.02	0.81	0.02	0.87	0.02	0.67	0.01
FeO	0.02	8.88	0.11	9.21	0.06	12.57	0.07	17.91	0.08	19.12	0.08	18.99	0.09
Fe_2O_3	0.02	1.21	0.01	1.47	0.01	0.93	0.01	1.02	0.00	0.33	0.00	–	–
MnO	0.02	0.42	0.02	0.53	0.02	0.68	0.02	0.84	0.02	0.83	0.02	0.83	0.02
MgO	0.01	15.12	0.06	14.87	0.06	14.48	0.06	24.65	0.07	23.83	0.07	23.89	0.07
CaO	0.01	19.98	0.07	19.37	0.07	17.00	0.04	1.69	0.02	1.56	0.02	1.61	0.01
Na_2O	0.01	0.32	0.01	0.35	0.01	0.37	0.01	0.04	0.01	0.05	0.01	0.02	0.01
K_2O	0.01	–	–	–	–	0.06	0.01	0.02	0.01	0.02	0.01	0.03	0.01
Cr_2O_3	0.02	–	–	–	–	–	–	–	–	–	–	0.02	0.01
Total		100.13	0.41	100.01	0.36	100.88	0.35	100.78	0.35	100.69	0.35	100.22	0.35
XEn		44		44		43		69		67		67	
XFs		14		15		21		28		30		30	
XWo		42		41		36		3		3		3	

	Ilmenite				Titanomagnetite					
Point	AC3-ox79		MV7-ox07		AC3-ox80		MV-7-ox06		AC3-ox81	
Type	Crystal clot		Microphenocryst		Crystal clot		Microphenocryst		Microlite	
	d.l. (wt%)	wt%	SD	wt%	SD	wt%	SD	wt%	SD	wt%	SD
SiO_2	0.02	–	–	–	–	0.06	0.01	0.11	0.01	0.14	0.01
TiO_2	0.07	45.34	0.38	45.86	0.38	18.45	0.24	16.50	0.23	18.69	0.07
Al_2O_3	0.01	0.27	0.01	0.32	0.01	2.36	0.03	2.49	0.03	1.99	0.02
Fe_2O_3	0.02	15.10	0.04	14.96	0.04	29.06	0.06	30.71	0.07	27.75	0.06
V_2O_3	0.06	0.70	0.05	0.51	0.05	0.43	0.05	0.78	0.05	0.65	0.03
Cr_2O_3	0.02	–	–	–	–	0.03	0.01	0.02	0.01	–	–
FeO	0.02	34.70	0.09	35.67	0.10	47.88	0.11	46.40	0.10	47.82	0.11
MnO	0.02	0.68	0.02	0.74	0.02	0.79	0.02	0.66	0.02	0.84	0.02
MgO	0.01	3.42	0.03	3.09	0.03	2.51	0.03	2.39	0.03	2.16	0.03
CaO	0.02	–	–	0.02	0.01	–	–	0.16	0.01	0.09	0.01
Total		100.20	0.62	101.15	0.64	101.56	0.56	100.23	0.56	100.12	0.36
XFeO		42		43		62		62		62	
XFe_2O_3		8		8		17		18		16	
$XTiO_2$		50		49		21		20		22	

For these and other pyroxene and Fe-Ti oxide analyses the values of FeO and Fe_2O_3 were obtained following the procedure of Putirka (2008) and Droop (1987), respectively.

preglacial QVC basaltic andesites (3.87 to 4.57), while Villarrica products show values of 1.94 to 2.87 (Fig. 4b). Huililco and QVC trace element patterns are similar to Lanín samples (Fig. 4), except for the slightly positive Zr anomaly in QVC. Strong Sr, P and Ti negative anomalies appear in all the trachytes (QVC and Lanín).

We provide 6 new Sr and Nd isotopic analyses for the QVC samples (see Supplementary material). We compare these data with available Sr and Nd isotopic ratios of the Villarrica, Quetrupillán and Lanín stratovolcanoes, as well as data from minor eruptive centers located north of the studied area (Fig. 5; Hickey-Vargas et al., 1989; Morgado et al., 2015). Although the stratovolcanoes and minor eruptive centers are clustered in a relatively small area of ca. 1200 km^2, there is an important dispersion of the isotopic ratios, being particularly large for the minor eruptive centres data. The QVC has a narrow compositional range in the $^{87}Sr/^{86}Sr$ ratios (0.70399 to 0.70402), whereas the $^{143}Nd/^{144}Nd$ ratios are more dispersed and range from 0.51279 to 0.51285. QVC isotopic ratios do not significantly differ from those of Lanín and Huililco, but exhibit lower $^{143}Nd/^{144}Nd$ ratios than Villarrica volcano.
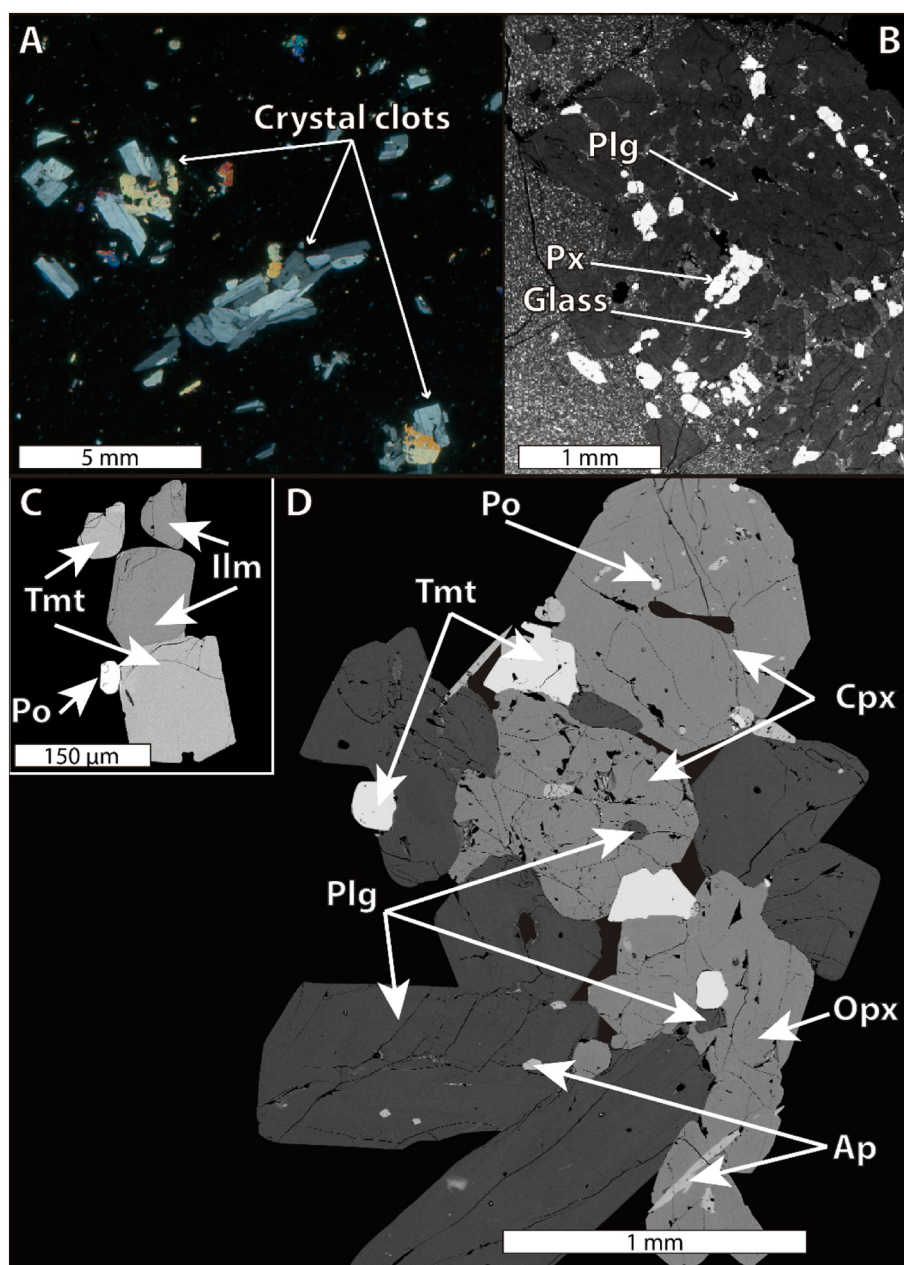
Fig. 2. (A) Crossed nicols photomicrograph of crystal clots (AC6-1 sample) within a glass-rich groundmass. (B) BSE image of a crystal clot with strong resorption features and glassy veins (MV2 sample). (C) BSE image of a Fe-Ti oxide pair of a QVC trachyte sample. (D) BSE image of a crystal clot of a QVC trachyte sample, which contains all phenocryst phases found in these lava samples, with the exception of ilmenite. Ap = apatite, Cpx = clinopyroxene, Opx = orthopyroxene, Plg = plagioclase, Po = pyrrhotite, Tmt = titanomagnetite, Ilm = ilmenite. The groundmass surrounding the clot is extremely glassy.

6. Mineral chemistry

Mineral compositions from QVC trachyte samples are listed in the Supplementary material. Representative analyses are shown in Table 2.

Pyroxene phenocrysts, mostly forming crystal clots, are augites with a narrow compositional range of $En_{42-47}Fs_{12-19}Wo_{38-42}$ and enstatites of $En_{64-68}Fs_{28-32}Wo_{03-04}$, whereas the microlites have a wider compositional range of $En_{38-67}Fs_{18-35}Wo_{03-40}$ (Fig. 6). Assuming the whole-rock composition of the nearly aphyric trachyte as the melt composition, clinopyroxene phenocrysts are mostly in slight disequilibrium with the melt composition, based on the clinopyroxene-melt equilibrium test of Putirka (2008), and orthopyroxene phenocrysts are mostly in equilibrium with both the whole rock composition and clinopyroxene crystals (Fig. 8a; based on the orthopyroxene-melt and clinopyroxene-orthopyroxene equilibrium tests of Putirka, 2008, respectively).

Ti-magnetite phenocrysts (considered as solid solution between ulvöspinel and magnetite, Fe_2TiO_4 and Fe_3O_4, respectively) have a wide compositional range of $Usp_{64-86}Mgt_{14-34}$, similar to the microlites ($Usp_{67-86}Mgt_{14-33}$), but ilmenite (considered as solid solution between ilmenite and hematite, $FeTiO_3$ and Fe_2O_3, respectively) phenocryst compositions have a narrow range ($Ilm_{90-94}Hmt_{6-10}$). Fe-Ti oxide phenocrysts mostly occur as both isolated microphenocrysts or microphenocryst in-contact pairs (Fig. 2c), although they are also found in crystal clots as inclusions.

Three groups of plagioclase phenocrysts were identified. Group 1 consists of plagioclase phenocrysts up to 3.4 mm long and with oscillatory zoning between An_{40-50} (Fig. 7a and b). They also appear as part of crystal clots that include pyroxene crystals. Group 2 includes phenocrysts of similar size to those of Group 1 (Fig. 7c to f) and they are found mainly as single crystals. They are also found (in less extent) as part of crystal clots, but
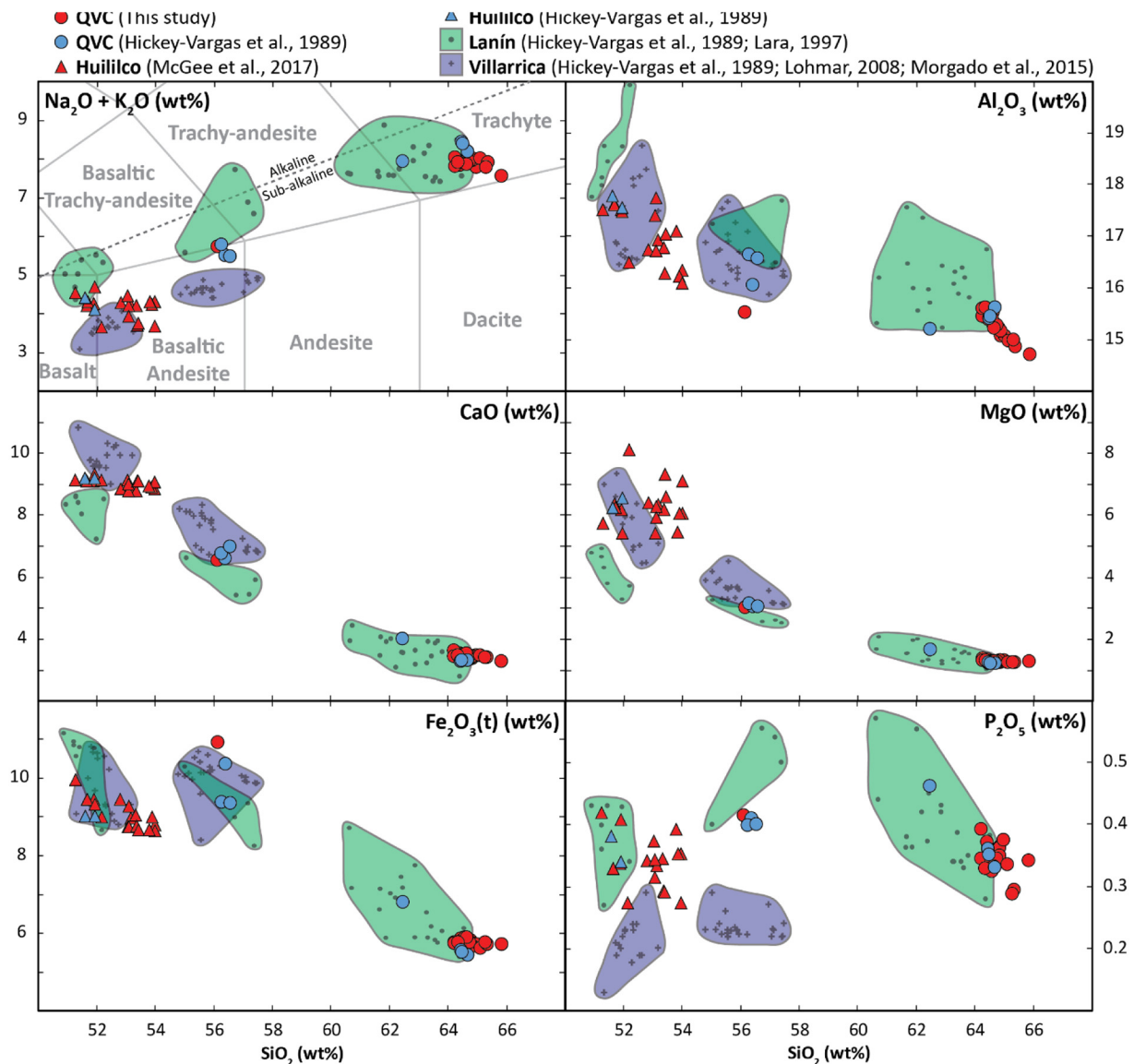
Fig. 3. TAS and major elements Harker diagrams for analyzed samples and those obtained from the literature (Hickey-Vargas et al., 1989; Lara, 1997; Lohmar, 2008; McGee et al., 2017; Morgado et al., 2015).

not in pyroxene-bearing crystal clots. Group 2 plagioclases have more mafic cores (An$_{70-85}$) surrounded by rims of An$_{40-50}$ with oscillatory zoning. Rims are ca. 100 μm to 400 μm thick, and transition from core to rim is gradual or sharp. Partially resorbed anorthite-poor cores of An$_{40-55}$ (similar to the Group 1 plagioclase compositions) surrounded by the An$_{70-85}$ zones, are commonly observed (Fig. 7d to f). Group 3 includes the smallest (<1 mm) phenocrysts, commonly adhered to bigger plagioclase crystals (Fig. 7a and d). These crystals are nearly unzoned with composition of An$_{40-45}$ similar to Group 1 phenocryst and Group 2 resorbed cores or oscillatory rim compositions. Group 1 comprises about 70 vol% of all plagioclase phenocrysts in the trachytes, Group 2 comprises about 25 vol% of the total amount of plagioclase phenocrysts, while the remaining 5 vol% includes the Group 3 plagioclases. All three plagioclase groups are found throughout the trachytic samples.

7. Thermometry and oxybarometry

The two-pyroxene geothermometer of Putirka (2008) (Eq. (36); after Brey and Kohler, 1990) was used to calculate temperatures from 40 augite-enstatite pairs that passed the equilibrium test of Putirka (2008) (Fig. 8a). Because the uncertainties in calculated pressures of the two-

pyroxene barometer from Putirka (2008) are high (±3.7 kbar), a pressure value of 0.8 kbar was chosen for the temperature calculation. This value was taken from the best fit results of the rhyolite-MELTS fractional crystallization simulations (see below). Even so, the augment of the temperature estimates with increasing pressure values is low (ca. 4 °C every 1 kbar). Pyroxene pairs from crystal clots give temperatures between 920 ± 55 °C and 960 ± 55 °C, whereas the isolated pyroxene phenocryst pairs give temperatures between 895 ± 56 °C and 930 ± 55 °C (Fig. 8c).

Forty-four core compositions of ilmenite – Ti-magnetite in-contact pairs (Fig. 2c) that passed the Mg-Mn equilibrium test of Bacon and Hirschmann (1988) (Fig. 8b) were used to calculate T and fO_2 estimates. The results from the thermometer of Ghiorso and Evans (2008) are between 965 ± 20 °C and 1115 ± 20 °C, similar to the results from the Sauerzapf et al. (2008) thermometer (960 ± 50 °C to 1115 ± 50 °C). These estimates cover a wide range of temperatures, however, most temperatures are higher than 1000 °C (Fig. 8c). The calculated fO_2 values vary between −0.1 ± 0.3 ΔNNO and 0.6 ± 0.3 ΔNNO using the Ghiorso and Evans (2008) method, and between 0.2 ± 0.4 ΔNNO to 0.8 ± 0.4 ΔNNO using the Sauerzapf et al. (2008) method (NNO values after O'Neill and Pownceby, 1993). Fugacity and temperature estimates do not correlate with crystal size or occurrence as free crystals or crystal clots.
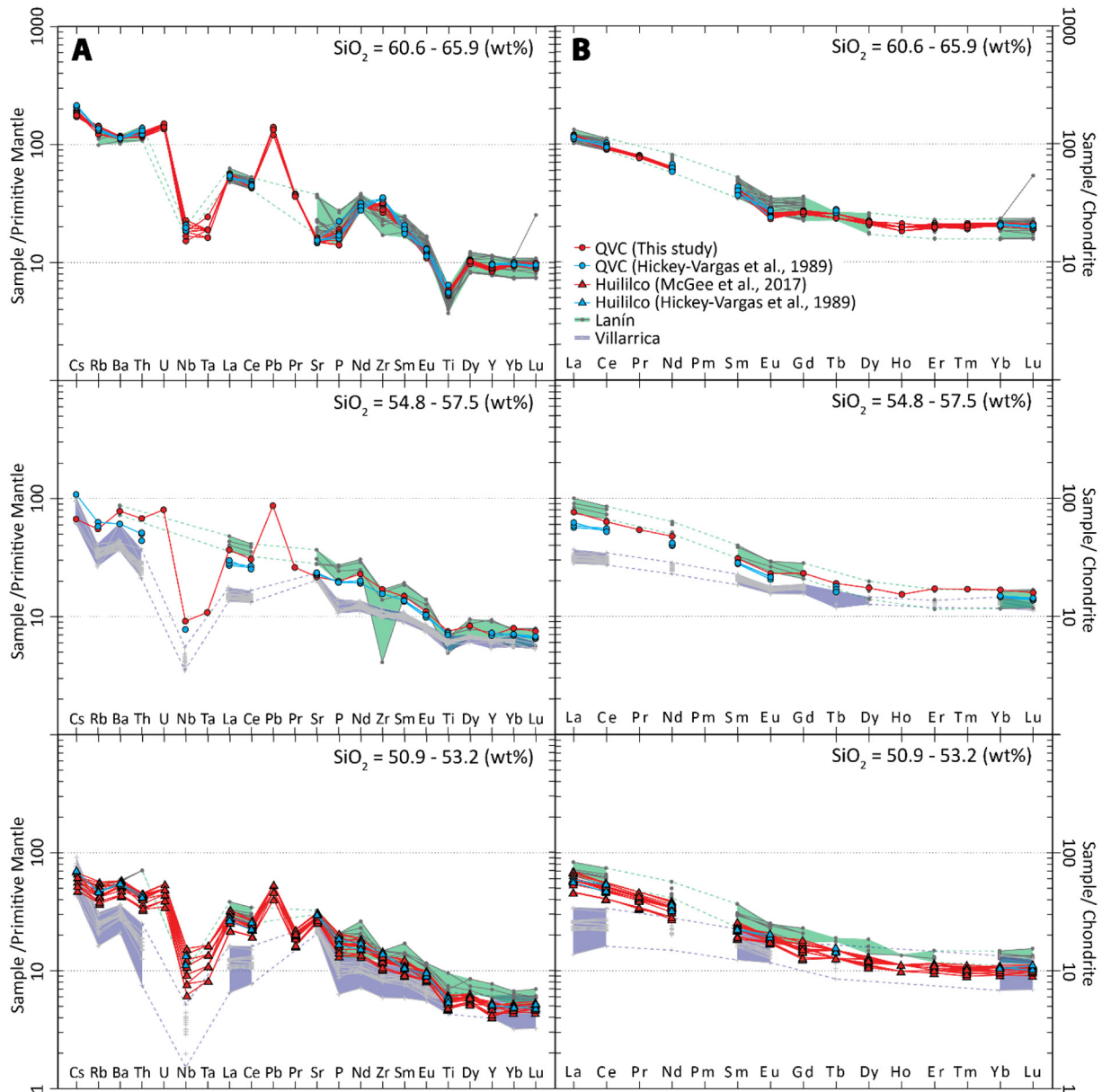
Fig. 4. (A) Spider diagrams normalized to the primitive mantle composition from McDonough and Sun (1995) and (B) REE diagrams normalized to the chondrite composition of Boynton (1984). The diagrams are divided in high-, mid- and low-SiO₂ groups. Huililco data is from McGee et al. (2017). Villarrica and Lanín data were taken from Hickey-Vargas et al. (1989), Lara (1997), Lohmar (2008) and Morgado et al. (2015).

8. Discussion

8.1. Generation of QVC trachytes: residual melt of basalt differentiation

8.1.1. Insight from PER diagram analysis

We consider Huililco basalts as representative of the initial melt compositions to generate QVC trachytes by fractional crystallization because of the following reasons. First, the magmas share geographic proximity, and may share a common plumbing system (eg., McGee et al., 2017). Second, the Huililco basalts are more mafic than the QVC samples (Fig. 3), but share similar isotopic signatures, unlike other small eruptive centers of the area (Fig. 5).

Fig. 9 shows a PER diagram in which Zr and K are conservative elements, because they approximate to a straight line that intersects the origin when plotted again each other (Pearce Element Ratios; Pearce, 1968; Russell and Nicholls, 1988; Stanley and Russell, 1989). Thus, if Huililco compositions generated the QVC trachytes by fractional crystallization,

K and Zr are not fractionated by any mineral crystallization and they are not added by processes of crustal assimilation. The absence of biotite, amphibole, K-feldspar and zircon is consistent with unmodified contents of K and Zr. The slightly positive Zr anomaly in the QVC trachytes may also indicate an absence of zircon fractionation (Fig. 4). The PER assemblage test diagram of Fig. 9b indicates that fractionation of a plagioclase + clinopyroxene + olivine + Ti-magnetite + apatite (all phases seen in the QVC trachytes and Huililco basalts) could explain the generation of the QVC trachytes from a parental magma of the Huililco-type composition. These results agree with the strong negative anomalies in Sr, P and Ti observed in the QVC trachytes (Fig. 4). Fractionation of orthopyroxene in trachytes is not detected in Fig. 9b, probably because its proportion is by far smaller than the sum of the other phases. The cationic proportion of orthopyroxene needed to significantly displace the fractionation path from QVC basaltic andesite to the QVC trachytes should be higher than 25% of total fractionated mineral phases (Fig. 9b), which is considerably higher than the proportion seen in the trachytes petrography.
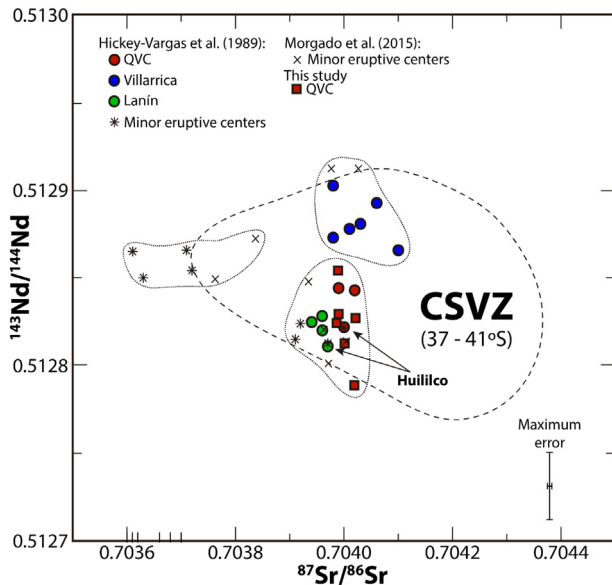
Fig. 5. Sr and Nd isotopic ratios of the volcanic systems near the studied area, taken from Hickey-Vargas et al. (1989), Morgado et al. (2015) and new data of QVC trachytes. The dashed line encloses the Central South Volcanic Zone (CSVZ; López-Escobar et al., 1995). Error bars showed indicate the maximum errors for the data of both isotopic ratios (see Supplementary material).

8.1.2. Simulations of magma differentiation

Simulations by rhyolite-MELTS software of fractional crystallization followed by equilibrium to reproduce the QVC trachytes were performed (Ghiorso and Gualda, 2015; Gualda et al., 2012) using the Huililco basalt sample as the initial composition (LEM-8A from McGee et al., 2017; Table 1). The simulations were separated into two stages (Fig. 10). Stage 1 corresponds to fractional crystallization from a Huililco-type composition (LEM-8A) to reproduce QVC preglacial basaltic andesites (samples PG1 and Q1–3; Table 1 and Hickey-Vargas et al., 1989) and Stage 2 consists of equilibrium crystallization from the mentioned preglacial basaltic andesites to reproduce the QVC trachyte compositions. PG1 and Q1–3 samples correspond to the QVC basaltic andesite composition with the lowest and highest Al_2O_3 content, respectively. Simulations were performed under isobaric conditions at different pressures (0.5 to 5 kbar). QFM and NNO oxygen buffers were used, because the Fe-Ti oxide oxybarometry results are closer to the NNO buffer conditions; however, simulations under the QFM buffer better reproduces the Fe-Ti oxide compositions. Both oxygen buffers are similar, NNO buffer representing a little higher fO_2 values (e.g., NNO at temperature - pressure conditions of 1000 °C - 1 kbar is equivalent to a ΔQFM value of 0.71). This could be explained by the fast re-equilibration of Fe-Ti oxides (see below), which could record higher fO_2 conditions than the pre-eruptive conditions through partial re-equilibration during eruption. The best fit for the QVC basaltic

andesite compositions were reproduced at 0.8 and 0.65 kbar for QFM and NNO buffers, respectively (Fig. 10a). These low pressure estimates for the QVC magmatic chamber are consistent with the 3 km to 4 km depth estimates done by Pavez (1997), through analysis of the superficial features of the caldera geometry.

The main fractionated phases during the whole crystallization process are plagioclase, olivine and clinopyroxene with small amounts of Ti-magnetite and low-Ca pyroxenes. Olivine crystallization occurs only during Stage 1, consistent with its absence in the trachytic samples. Under QFM buffer conditions, crystallization of low-Ca clinopyroxene over orthopyroxene was favoured, while under NNO buffer, small amounts of orthopyroxene were reproduced. Details of compositions and weight fraction of the crystallizing phases are included in Supplementary material. The excess of Ca in the trachytes from the simulations compared to the QVC samples are explained by the absence of apatite in the fractionated phases of the rhyolite-MELTS simulations. Given that an increase of H_2O concentration in magmas inhibits plagioclase crystallization by lowering its liquidus temperature, an increase of Al_2O_3 content in the melt is expected (Almeev et al., 2012). The observed variations of Al_2O_3 content (>1 wt%) in QVC basaltic andesites are reproduced from H_2O content variations of H_2O-undersaturated QVC melt between 0.65 and 1.20 wt% H_2O (Fig. 10a). These variations could result from injection of magma batches with different volatile content, changing the volatile proportion with each new batch. When reaching trachytic compositions, the melt reaches water saturation by equilibrium crystallization in the Stage 2 simulation at ca. 2.9–3.3 wt% H_2O (Fig. 10a). From this point forward, H_2O exsolution progress as crystallization continues. The gradual loss of H_2O in the melt produces an increase in plagioclase crystallization, causing the change observed in the Al_2O_3 Harker diagram slope, toward lower Al_2O_3 concentrations in the residual trachytic melt. The hygrometer from Waters and Lange (2015) was used to evaluate the saturation water contents of the trachytes obtained with the rhyolite-MELTS simulations (2.9 wt% to 3.3 wt% H_2O). To obtain a complete range of water content results, the trachytic sample compositions of this study with the lowest and highest SiO_2 concentrations were selected for the calculations (AC5-2 and MV1; see Supplementary material). Temperatures of 920 °C and 960 °C, pressures of 0.65 kbar and 0.80 kbar and plagioclase compositions of An_{40} and An_{50} were used. Consistent estimates between 2.4 wt% and 3.6 wt% H_2O were obtained.

With the aim of confirming the results from the rhyolite-MELTS simulations, modeling of trace element distribution was also performed (Fig. 10b; the selected Kd's are given in the Supplementary material). Mineral phase proportions consistent with the simulations results were chosen for the trace element models. Stage 1 and 2 were successfully reproduced, obtaining the trace element content of PG1 sample starting from LEM-8A sample as initial composition (Stage 1), and obtaining the composition of AC7-B sample from the initial composition of PG1 (Stage 2). A total of 67 wt% crystal fractionation is needed for the generation of the QVC trachytes from Huililco basalts (40 wt% fractionation from Stage 1 plus an extra 27 wt% fractionation from Stage 2), consistent with the crystal fractionation proportions obtained from the rhyolite-MELTS simulations (between 64 wt% and 73 wt% fractionation; see Supplementary material).

8.2. Rejuvenation of a highly crystalline trachytic reservoir

We interpret the abundance of crystal clots within crystal-poor QVC trachytes as testimony of a dismembered crystal network from a mush system, consistent with QVC compositional gaps (Fig. 4; Dufek and Bachmann, 2010). As a consequence of compaction of solid phases, crystal clot-bearing interstitial melts could be extracted from the mush giving rise to the studied QVC trachytes (Bachmann and Bergantz, 2004; Hildreth, 2004). Additionally, the observed compositional homogeneity of the QVC trachyte melts (64.2–65.8 wt% SiO_2) and its minerals (e.g. pyroxene composition; Fig. 6) would result from near-equilibrium crystallization associated with mush formation where crystallization of
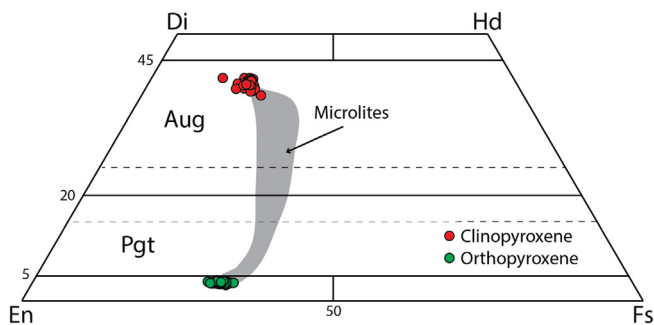

Fig. 6. Pyroxene phenocryst (both crystal clots and isolated phenocrysts) compositions of the QVC trachytes. The grey area indicates the compositional range of pyroxene microlites.
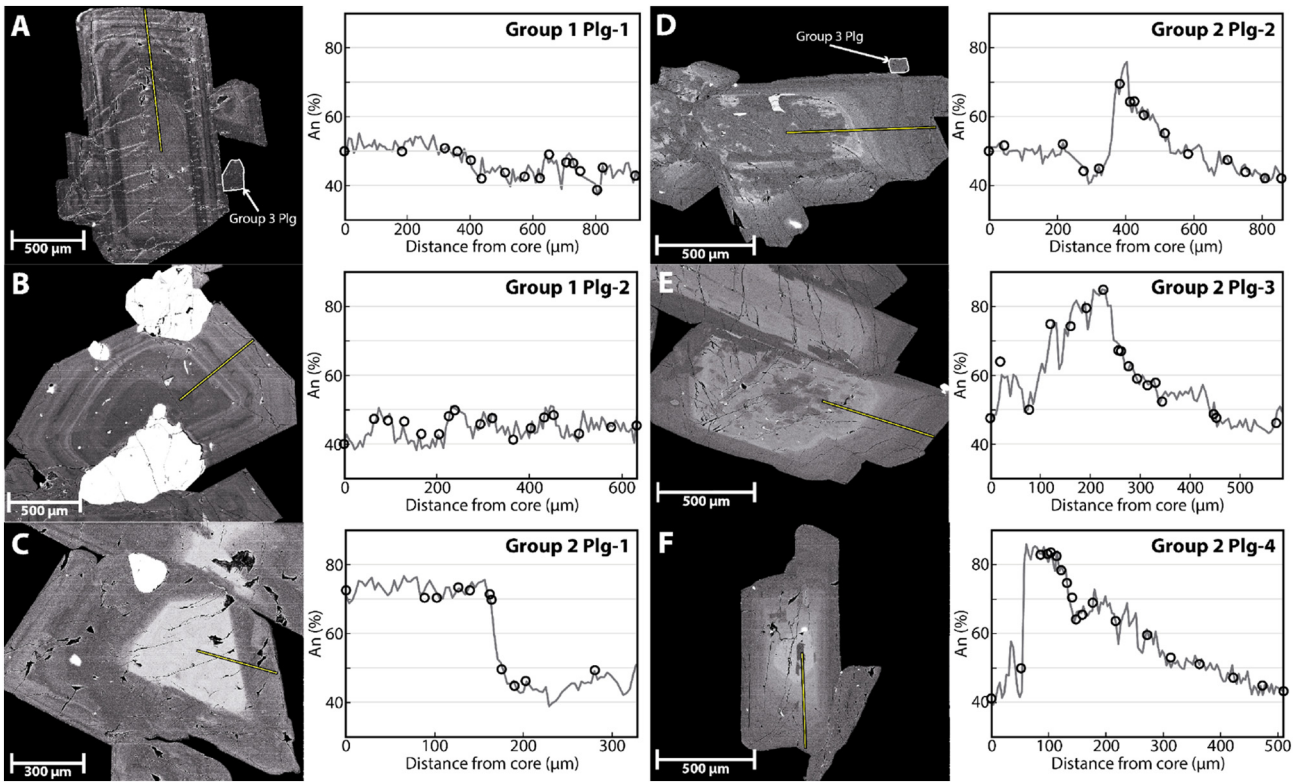
Fig. 7. BSE images and anorthite compositional profiles of selected plagioclase phenocrysts from Group 1 and Group 2 plagioclase phenocrysts. Circles in the compositional profiles are the anorthite content obtained from the EMPA analyses and the grey lines are the calibrated grey scale profiles from the BSE. (A) and (B) are oscillatory plagioclase from Group 1. (C) to (F) are plagioclase phenocrysts from Group 2. Note that plagioclase in (C) has a sharp transition to the outer rim, while those of (D) to (F) present an albitic internal core with resorption features and a smooth transition to the outer rim.

Fig. 8. (A) Clinopyroxene-orthopyroxene equilibrium test (Putirka, 2008) of the pyroxene pairs used for geothermometry. (B) Titanomagnetite-ilmenite Mg-Mn equilibrium test (Bacon and Hirschmann, 1988) of the Fe-Ti oxide pairs used for geothermometry. (C) Temperatures obtained by geothermometry of two-pyroxene (Putirka, 2008) and Fe-Ti oxides (Ghiorso and Evans, 2008) for each lava sample analyzed in EMPA. Green circles are the calculated temperatures from pyroxene pairs in crystal-clots, while white circles are from isolated pyroxene pairs. Blue circles are from Fe-Ti oxide pairs. Solid lines include all temperatures within the calculated maximum and minimum values. Dashed lines indicate the maximum and minimum error.
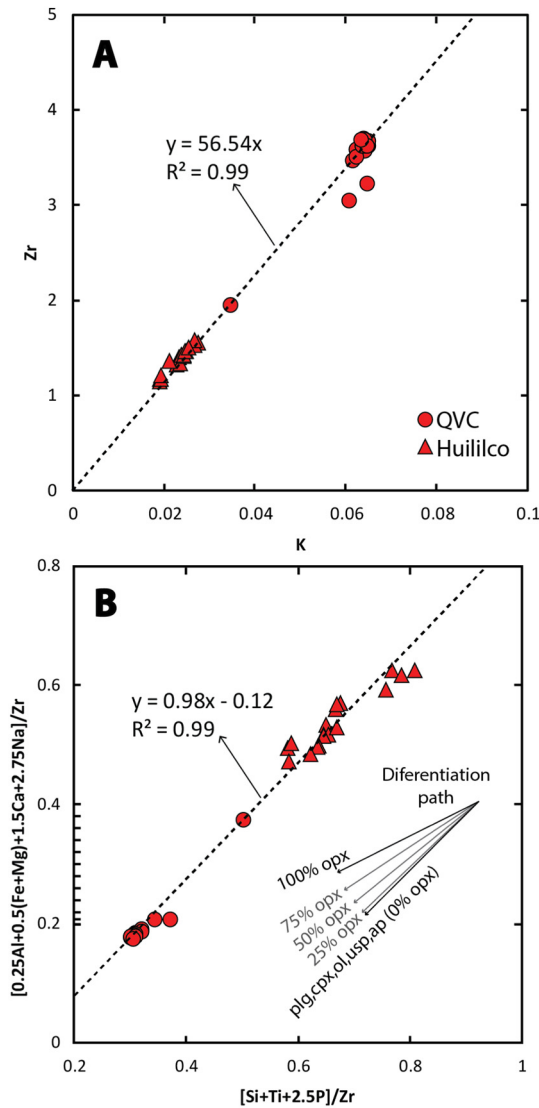
Fig. 9. (A) PER (Pearce element ratios) conservative elements test for K and Zr. (B) PER assemblage test diagram showing the effect of plg + cpx + ol + usp (ülvospinel) + ap phase assemblage to reproduce the studied sample compositions distributed along a well-constrained line with slope = 1. The effect of opx fractionation is also shown (cation percentages of total fractionated phases). Triangles are the Huililco samples from McGee et al. (2017) and circles are the QVC samples from this study.

temperatures estimates are representative of the conditions of crystal mush rather than those of the accumulation zone.

Equilibrium clinopyroxene compositions and rhyolite-MELTS modeling indicate the pre-eruptive storage conditions of the QVC crystal mush were likely ca. 940 ± 75 °C and <1 kbar (the higher Fe-Ti oxide temperature estimates are discussed below). Plagioclase zonation patterns and the presence of partially resorbed crystal clots crossed by glassy veins (Fig. 2b) provide evidence of incomplete dissolution-reaction-reprecipitation process (Cashman and Blundy, 2013). These incongruent dissolving textures give us insights into the rejuvenation of the crystal mush by heating of the trachyte reservoir. The An_{70-85} intermediate zone of Group 2 plagioclase phenocrysts was formed under conditions of higher temperatures and lower SiO_2 content than the partially resorbed core (An_{40-55}) commonly present (because of the saturated state of the trachytes, water addition is not a relevant factor in plagioclase composition). The formation of the An_{40-50} oscillatory rims around the An-rich zone of all Group 2 plagioclase phenocrysts indicates the restoration of conditions similar to those of the resorbed cores. Assuming that the crystal mush rejuvenated by the arrival of hot magma from below, the resorbed cores of Group 2 plagioclase crystals are interpreted as the remnants of crystals formed in the mush at the same conditions of the Group 1 plagioclase crystals before heating. Rejuvenation implies opening of the crystal network and upward transport of Group 2 plagioclase to the melt accumulation zone, where the previous conditions are restored allowing An_{40-50} rims to grow.

Two nonexclusive extreme mechanisms of heating are discussed to explain the changing conditions of the QVC trachyte reservoir. If a new magma batch stalls just below the crystal-rich reservoir, the resulting heat (and H_2O) transfer would melt the crystal network generating closed-system mixing between the interstitial melt and the melted crystal network (e.g. Kent et al., 2010; Fig. 11b), thus more mafic melts are available favouring regrowth of the An_{70-85} zones (Fig. 11c). A simulation of mixing between the interstitial melt (represented by the whole-rock trachytic composition of sample AC7-B) and the melt composition equivalent to the crystal clot composition (representative of the crystal network; see Appendix A for details on the calculation of the clot composition) was performed to test if this closed system model is sufficient to generate the An_{70-85} zones of plagioclase crystals. The resulting melt compositions obtained from mixing between trachyte and crystal clot-derived melt compositions (after modal fusion) can reproduce An_{70-85} plagioclase compositions when the crystal fraction is around the extraction window (where crystal-liquid separation takes place most efficiently, 50% to 70% crystallinity; Dufek and Bachmann, 2010; Fig. 12a). The less anorthitic plagioclase core compositions (An_{70}) of Group 2 plagioclase phenocrysts are reproduced from a melt of 50 wt% mixing at ca. 1010 °C (i.e. 50–90 °C higher than the 920–960 °C calculated from the two-pyroxene thermometer in crystal clots), but the most anorthitic Group 2 plagioclase core composition (An_{85}) is not reproduced, which could be indicative of some participation of the new hot magma batch in the mixing.

The second mechanism consists of the injection of a new magma batch into the crystalline reservoir allowing open-system mixing. Berganz et al. (2015) discussed that at low input rates a new and hot magma supply would produce magma intrusion and spreading into the crystal network, by displacing the residual melt or mingling between the two magmas. In this scenario the magma would interact with the crystal network creating domains where the Ca-rich zones of the Group 2 plagioclase crystals can grow. An analysis of trace element (Sr, Ba) content of the An rich zone of Group 2 plagioclase could aid to discriminate which of (or on what degree) these processes are involved. A plagioclase that crystallizes from a melt produced by fusion of other plagioclase would be enriched in Sr and Ba with respect to a plagioclase that crystallizes from a new basaltic magma input.

Regardless of which is the dominant mechanism of mixing, plagioclase crystals with An_{70-85} zones must be transported by ascending melts through the mush zone up to the accumulation zone (Fig. 11d).

trapped melts released abundant latent heat bringing the cooling rate close to zero (Huber et al., 2009). This interpretation is in agreement with the high degree of crystal fractionation (ca. 67%) deduced from the rhyolite-MELTS and trace element models.

As was discussed in previous sections, the equilibrium tests of Putirka (2008) indicates that clinopyroxene is in slight chemical disequilibrium with the melt, whereas orthopyroxene is in chemical equilibrium with the melt. These results appear to conflict with the clinopyroxene-orthopyroxene equilibrium test, which shows that most in-contact pyroxene pairs are in equilibrium with each other (Fig. 8a). These equilibrium tests can only be certain of disequilibrium (if the test is not passed) but they cannot confirm equilibrium conditions (if the test is passed). We interpret that both phases are in equilibrium with each other, because they are in contact since before disaggregation from the mush. In consequence, the time of equilibration within the clinopyroxene-orthopyroxene system is much higher than the time of equilibration with the final trachytic melt. Therefore, we conclude that both mineral phases are in slight disequilibrium with the melt. This interpretation also means that the pyroxene
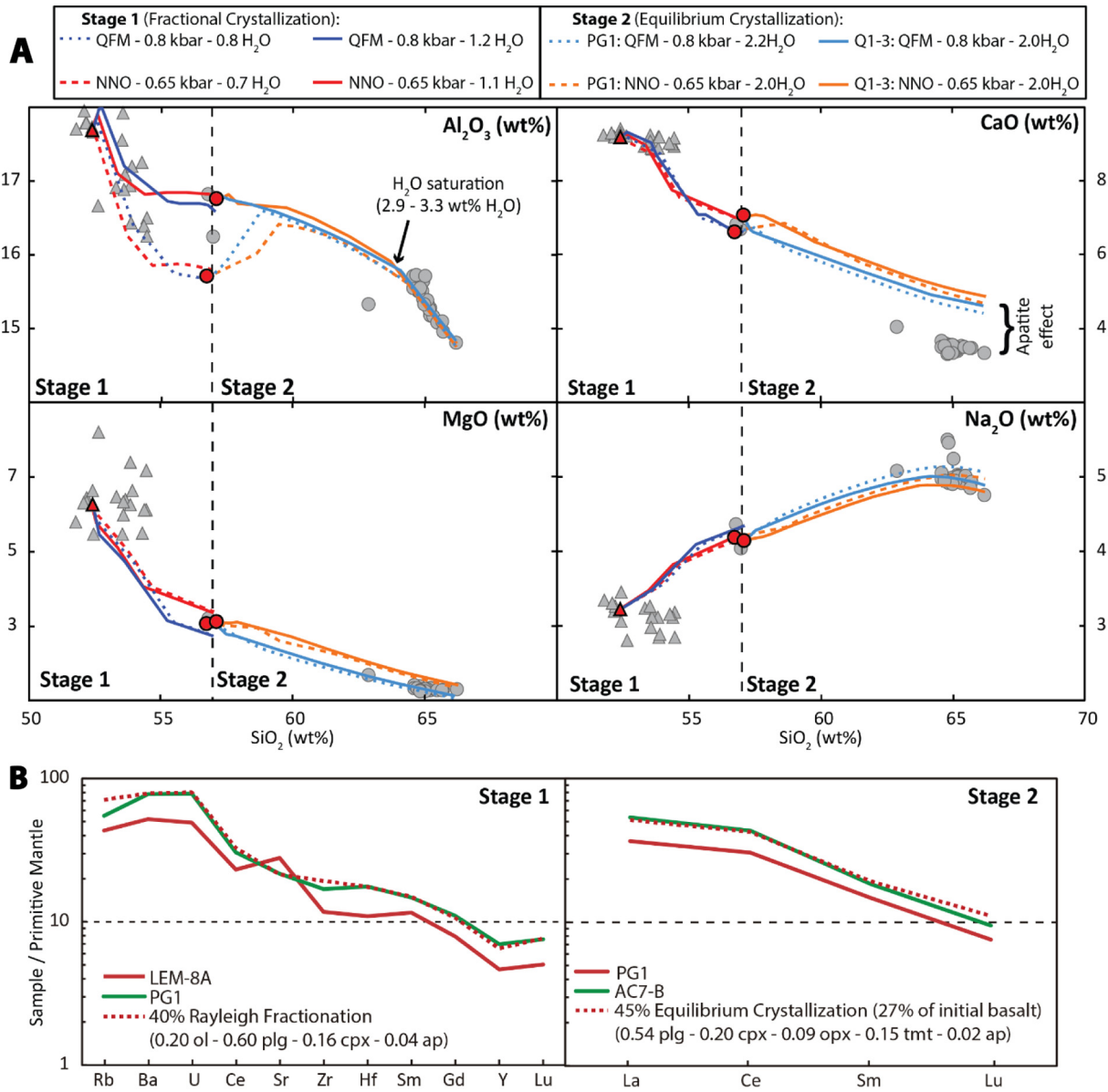
Fig. 10. (A) Harker diagrams showing the simulated evolution of the residual melt compositions by rhyolite-MELTS for stages 1 and 2 at different conditions of oxygen fugacity, pressure and water content. Red and light blue circles indicate the compositions of QVC samples from this study and Hickey-Vargas et al. (1989), respectively, while red and light blue triangles show the compositions of Huililco samples from McGee et al. (2017) and Hickey-Vargas et al. (1989), respectively. (B) Spider diagrams showing the results of the trace elements modes of fractional crystallization and equilibrium crystallization for stages 1 and 2, respectively. Primitive Mantle composition from McDonough and Sun (1995).

The proportion of mixed melt that was transported upward with suspended Group 2 plagioclase crystals should be low compared with the trachytic melt proportion, which could explain the restoration of An_{40-55} composition and the absence of strong disequilibrium textures in the other trachyte phenocryst phases.

8.3. Late heating event in the trachyte reservoir: an eruption trigger?

The higher temperatures of Fe-Ti oxide equilibria compared with those calculated from pyroxene composition (Fig. 8c) evidences the existence of a post-pyroxene heating event of ca. 155 ± 75 °C in the trachyte reservoir. To explain why this heating does not affect pyroxene composition, it is necessary to consider that Fe-Ti interdiffusion rates in Fe-Ti oxide phases are substantially faster than those of pyroxene Fe-Mg interdiffusion. For example, at 1000 °C diffusivity (D) at the NNO oxygen buffer conditions of Fe-Ti in Ti-magnetite (X_{Ti} = 0.2) is 5.6×10^{-16} m^2/s (Aragon et al., 1984; Van Orman and Crispin, 2010), while D of Fe-Mg

interdiffusion in clinopyroxene and orthopyroxene at 1000 °C is 1.9×10^{-20} m^2/s and 7.9×10^{-20} m^2/s, respectively (Müller et al., 2013). This means that the re-equilibration of Fe-Ti oxides after heating is four orders of magnitude faster than pyroxenes and if the time interval between heating and eruption is sufficiently short (such as in syn-eruptive heating), the heating will only be recorded in the Fe-Ti oxides. The observed wide range of temperatures of Fe-Ti oxides indicates that the temperature distribution upon heating was not homogeneous, probably because the homogenization was interrupted as a consequence of eruption. This heating event cannot be associated with the formation of the An_{70-85} zones in the Group 2 plagioclase, because these plagioclases needed a longer time between heating and eruption to re-equilibrate and regrowth at the lower temperatures represented by the Group 2 plagioclase rims of An_{40-50}. Heating events of this scale, which lead to eruption, have already been propose for other volcanic systems in the Southern Volcanic Zone of the Andes, e.g. the ca. 130 °C reheating in Quizapu volcano (Ruprecht and Bachmann, 2010) or the ca. 200 °C
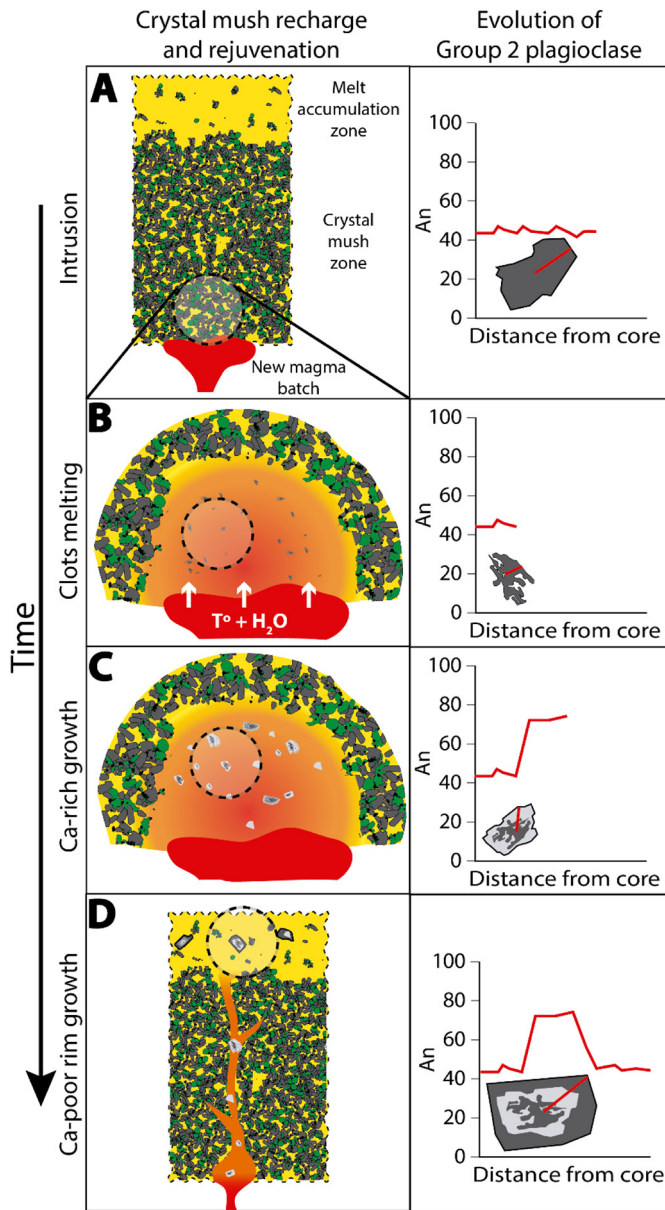
Fig. 11. Conceptual model of Group 2 plagioclase phenocryst formation as a consequence of arrival of a new and hot mafic magma batch. The interaction between the mush zone and the new magma input, and the resulting plagioclase textures are also shown. The figures on the right show the schematic evolution of Group 2 plagioclase phenocrysts. The dashed circles show the location of the Group 2 plagioclase crystals at each evolutionary stage. (A) The new magma batch stalls below the mush zone. (B) Melting in the mush zone of crystal clot mineral assemblage caused by heating and water addition from the new magma batch (mixing with the new magma batch can also occur). (C) Regrowth, around partially resorbed plagioclase, of Ca-rich zones from a liquid generated by trachytic melt + melted clot composition (+ recharge magma). (D) Upward migration of the hybridized melt carrying Group 2 plagioclase phenocrysts. Restoration of the conditions of Group 2 plagioclase core composition takes place at the upper level of the trachyte melt-rich reservoir.

reheating in Villarrica volcano prior the Licán Ignimbrite eruption (Lohmar et al., 2012).

9. Conclusions

Whole rock mayor and trace element compositions, in addition to Sr and Nd isotopic ratios, suggest that QVC and the nearby Huililco small eruptive centre are genetically related. Rhyolite-MELTS and trace elements crystal fractionation models show that basalts with composition equivalent to Huililco products generated the trachytes, after ca. 67% crystallization. During the evolution of the magma, the water content
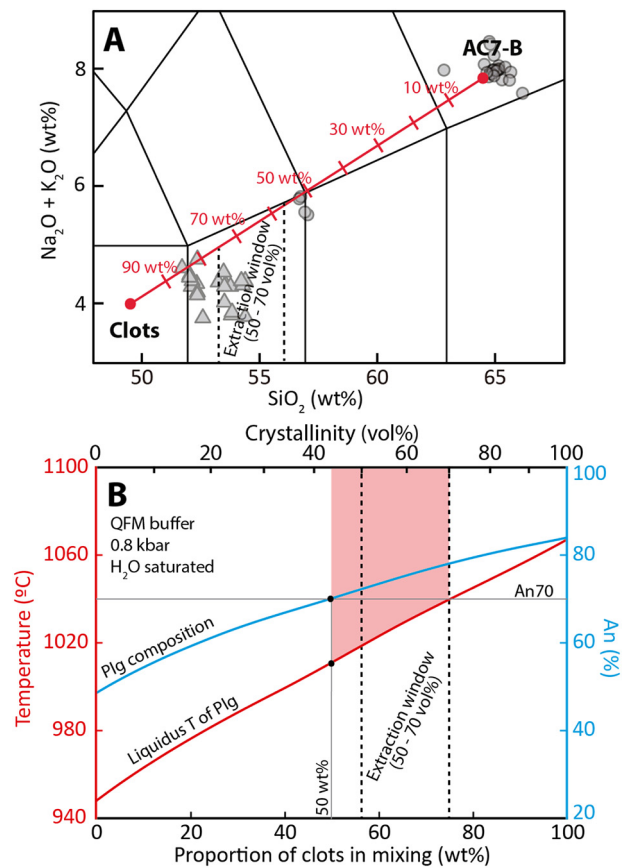

Fig. 12. (A) TAS diagram showing mixing between the interstitial trachytic melt (sample AC7-B; Supplementary material) and different proportions (wt%) of crystal clot composition. (B) Rhyolite-MELTS results of plagioclase liquidus (red line) for different mixing proportions and composition of plagioclase (light blue line) at the liquidus temperature. Melt extraction window (Dufek and Bachmann, 2010) is also shown. Red area indicates the possible temperatures and mixing proportions to produce melting of plagioclase and then regrowth of $>An_{70}$ (Group 2 plagioclase An-rich cores).

was variable, affecting plagioclase crystallization, but undersaturated volatile conditions remained. Volatile saturation did not occur until trachytic compositions were reached (~2.9–3.3 wt% H_2O). The low water contents are also consistent with the absence of hydrated mineral phases in the lava samples.

Textural evidence in the QVC trachytes suggests that the reservoir consists of a highly crystalline mush reservoir below a trachytic melt accumulation zone. The crystalline mush storage conditions are constrained by two-pyroxene thermometry (between 920 ± 55 °C and 960 ± 55 °C) and the rhyolite-MELTS simulations (>1 kbar). Shallow depths for the QVC magma chamber have been already proposed, based on the superficial geometry of the caldera. Two distinct events of recharge and remobilization of the mush are recorded in plagioclase and Fe-Ti oxide phenocrysts compositions. Complex zoning in some plagioclase phenocrysts shows melting and regrowth caused by heating and/or mixing with a new mafic melt. This process was followed by restoration of the initial storage conditions, which was achieved by migration of the affected plagioclase crystals to the upper melt accumulation zone. A more exhaustive analysis of trace element zonation profiles in plagioclase could clarify if the recharge involved mixing with the mush zone or if the new magma batch stalled below and mostly transferred heat and volatiles to the upper mush zone. Fe-Ti oxide temperatures record a second heating event of ca. 155 °C, which is probably the eruption trigger, because this late heating event must have been followed by rapid eruption as it did not widely affect other mineral phase equilibria.

Appendix A. Estimation of clot composition

The volume fraction of phases in crystal clots was measured by the point counting procedure, applied to circular polarized scanned thin sections. Apatite, which occurs in very small amounts as tiny crystals, was neglected. All the opaque crystals are assumed to be Ti-magnetite because ilmenite is scarce and it cannot be differentiated from Ti-magnetite from the scans. Clinopyroxene and orthopyroxene are taken as one phase in this stage. The point counting results are quite homogeneous and the average result is used for the composition estimation (Fig. A1; Table A1).

The densities are obtained from the rhyolite-MELTS simulations at the estimated mush conditions (Table A1). These densities are used to calculate the mass fraction of the phases in the clots as follows:

$$v_{plg} + v_{px} + v_{tmt} = 1$$

$$v_{plg}\delta_{plg} + v_{px}\delta_{px} + v_{tmt}\delta_{tmt} = M$$

$$v_{plg}\delta_{plg}/M + v_{px}\delta_{px}/M + v_{tmt}\delta_{tmt}/M = m_{plg} + m_{px} + m_{tmt} = 1$$

where v_x, δ_x and m_x are the volume fraction, density and mass fraction of the phase x, respectively. Pyroxene mass proportion is assumed to be 0.20 clinopyroxene and 0.06 orthopyroxene from SEM analysis. The density of clinopyroxene was used for the pyroxene phase because it is the most abundant pyroxene phase in the clots. Small variations in the cpx-opx fraction do not have a strong effect on the composition results.

A representative composition of each phase is chosen from the EMPA data (MV3-pl17, AC6-1-px86, AC6-1-px85 and AC3-ox80; Table 2). The selected plagioclase composition represents the mean value of Group 1 plagioclase and Group 2 plagioclase rims.

The major element compositions of the crystal clots are calculated as follows:

$$C^x_{plg}m_{plg} + C^x_{cpx}m_{cpx} + C^x_{opx}m_{opx} + C^x_{tmt}m_{tmt} = C^x_{clot}$$

where C^x_y is the wt% of the mayor element x in the phase. The clots composition estimation result is shown in Table A1.

Table A1
Mass average of phases in crystal clots, calculated from the volumes measured with point counting technique, and densities of this phases. Final clot composition results are also shown.

	Plg	Px	Ox
Volume average	0.705	0.231	0.640
Density (gm/cm³)	2.620	3.310	4.690
Mass average	0.634	0.263	0.103

	SiO₂	Al₂O₃	TiO₂	FeOₜ	MnO	MgO	CaO	Na₂O	K₂O
Calculated clot composition (wt%)	49.58	18.19	2.07	11.04	0.21	4.81	10.10	3.79	0.21

Appendix B. Supplementary data

Supplementary data to this article can be found online at https://doi.org/10.1016/j.jvolgeores.2018.04.020.

References

Almeev, R.R., Holtz, F., Koepke, J., Parat, F., 2012. Experimental calibration of the effect of H2O on plagioclase crystallization in basaltic melt at 200 MPa. Am. Mineral. 97: 1234–1240. https://doi.org/10.2138/am.2012.4100.
Aragon, R., McCallister, R.H., Harrison, H.R., 1984. Cation diffusion in titanomagnetites. Contrib. Mineral. Petrol. 85:174–185. https://doi.org/10.1007/BF00371707.
Bachmann, O., Bergantz, G.W., 2004. On the origin of crystal-poor rhyolites: extracted from batholithic crystal mushes. J. Petrol. 45:1565–1582. https://doi.org/10.1093/petrology/egh019.
Bacon, C.R., Hirschmann, M.M., 1988. Mg/Mn partitioning as a test for equilibrium between coexisting Fe-Ti oxides. Am. Mineral. 73, 57–61.
Bergantz, G.W., Schleicher, J.M., Burgisser, A., 2015. Open-system dynamics and mixing in magma mushes. Nat. Geosci. 8:793–796. https://doi.org/10.1038/ngeo2534.
Berlo, K., Blundy, J., Turner, S., Hawkesworth, C., 2007. Textural and chemical variation in plagioclase phenocrysts from the 1980 eruptions of Mount St. Helens, USA. Contrib. Mineral. Petrol. 154:291–308. https://doi.org/10.1007/s00410-007-0194-8.
Boynton, W.V., 1984. Cosmochemistry of the rare earth elements: meteorite studies. Rare Earth Element Geochemistry. Elsevier B.V https://doi.org/10.1016/B978-0-444-42148-7.50008-3.
Brey, G.P., Kohler, T., 1990. Geothermobarometry in 4-phase lherzolites 2. New thermobarometers, and practical assessment of existing thermobarometers. J. Petrol. 31:1353–1378. https://doi.org/10.1093/petrology/31.6.1353.
Cashman, K.V., Blundy, J.D., 2013. Petrological cannibalism: the chemical and textural consequences of incremental magma body growth. Contrib. Mineral. Petrol. 166: 703–729. https://doi.org/10.1007/s00410-013-0895-0.
Davidson, J.P., Morgan, D.J., Charlier, B.L.A., Harlou, R., Hora, J.M., 2007. Microsampling and isotopic analysis of igneous rocks: implications for the study of magmatic systems. Annu. Rev. Earth Planet. Sci. 35:273–311. https://doi.org/10.1146/annurev.earth.35.031306.140211.
Droop, T.R.G., 1987. A general equation for estimating Fe3+ concentrations in ferromagnesian silicates and oxides from microprobe analyses, using stoichiometric criteria. Mineral. Mag. 51:431–435. https://doi.org/10.1180/minmag.1987.051.361.10.
Dufek, J., Bachmann, O., 2010. Quantum magmatism: magmatic compositional gaps generated by melt-crystal dynamics. Geology 38:687–690. https://doi.org/10.1130/G30831.1.

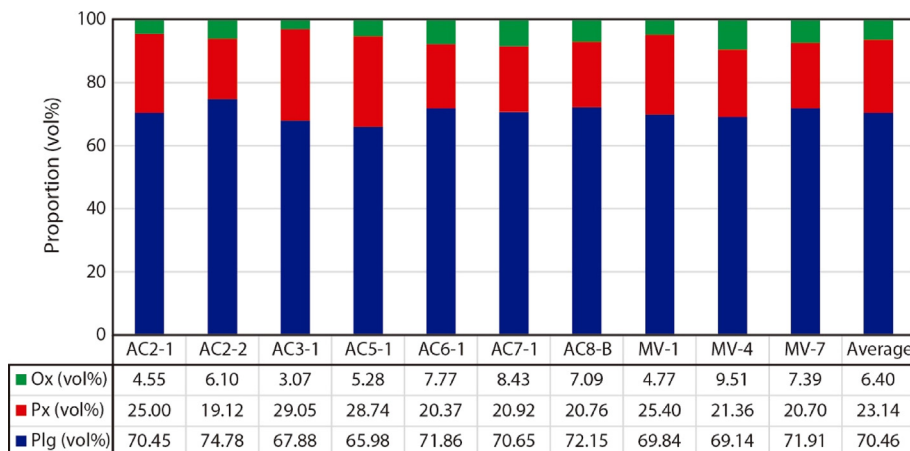|	AC2-1	AC2-2	AC3-1	AC5-1	AC6-1	AC7-1	AC8-B	MV-1	MV-4	MV-7	Average
Ox (vol%)	4.55	6.10	3.07	5.28	7.77	8.43	7.09	4.77	9.51	7.39	6.40
Px (vol%)	25.00	19.12	29.05	28.74	20.37	20.92	20.76	25.40	21.36	20.70	23.14
Plg (vol%)	70.45	74.78	67.88	65.98	71.86	70.65	72.15	69.84	69.14	71.91	70.46

Fig. A1. Point counting measurements of mineral volume proportion in crystal clots. Ox = oxides, Px = pyroxenes, Plg = plagioclase.

Ellis, B.S., Bachmann, O., Wolff, J.A., 2014. Cumulate fragments in silicic ignimbrites: the case of the Snake River Plain. Geology 42:431–434. https://doi.org/10.1130/G35399.1.

Ghiorso, M.S., Evans, B.W., 2008. Thermodynamics of rhombohedral oxide solid solutions and a revision of the Fe-Ti two-oxide geothermometer and oxygen-barometer. Am. J. Sci. 308:957–1039. https://doi.org/10.2475/09.2008.01.

Ghiorso, M.S., Gualda, G.A.R., 2015. An H2O–CO2 mixed fluid saturation model compatible with rhyolite - MELTS. Contrib. Mineral. Petrol. 169. https://doi.org/10.1007/s00410-015-1141-8.

Grove, T.L., Baker, M.B., Kinzler, R.J., 1984. Coupled CaAl-NaSi diffusion in plagioclase feldspar: experiments and applications to cooling rate speedometry. Geochim. Cosmochim. Acta 48:2113–2121. https://doi.org/10.1016/0016-7037(84)90391-0.

Gualda, G.A.R., Ghiorso, M.S., Lemons, R.V., Carley, T.L., 2012. Rhyolite-MELTS: a modified calibration of MELTS optimized for silica-rich, fluid-bearing magmatic systems. J. Petrol. 53:875–890. https://doi.org/10.1093/petrology/egr080.

Hickey-Vargas, R., Roa, H.M., López-Escobar, L., Frey, F.A., 1989. Geochemical variations in Andean basaltic and silicic lavas from the Villarrica-Lanin volcanic chain (39.5° S): an evaluation of source heterogeneity, fractional crystallization and crustal assimilation. Contrib. Mineral. Petrol. 103:361–386. https://doi.org/10.1007/BF00402922.

Hildreth, W., 2004. Volcanological perspectives on Long Valley, Mammoth Mountain, and Mono Craters: several contiguous but discrete systems. J. Volcanol. Geotherm. Res. 136:169–198. https://doi.org/10.1016/j.jvolgeores.2004.05.019.

Huber, C., Bachmann, O., Manga, M., 2009. Homogenization processes in silicic magma chambers by stirring and mushification (latent heat buffering). Earth Planet. Sci. Lett. 283:38–47. https://doi.org/10.1016/j.epsl.2009.03.029.

Huber, C., Bachmann, O., Dufek, J., 2011. Thermo-mechanical reactivation of locked crystal mushes: melting-induced internal fracturing and assimilation processes in magmas. Earth Planet. Sci. Lett. 304:443–454. https://doi.org/10.1016/j.epsl.2011.02.022.

Kent, A.J.R., Darr, C., Koleszar, A.M., Salisbury, M.J., Cooper, K.M., 2010. Preferential eruption of andesitic magmas through recharge filtering. Nat. Geosci. 3:631–636. https://doi.org/10.1038/ngeo924.

Lange, R.A., Frey, H.M., Hector, J., 2009. A thermodynamic model for the plagioclase-liquid hygrometer/thermometer. Am. Mineral. 94 (4):494–506. https://doi.org/10.2138/am.2009.3011.

Lara, L.E., 1997. Geología y geoquímica del Volcán Lanín (39.5°S/71.5°W), Andes del Sur, IX Región, Chile. (M.Sc. Thesis). Universidad de Chile, Chile.

Lara, L.E., Moreno, H., 2004. Geología del área Liquiñe-Neltume, regiones de Los Lagos y de La Araucanía. Servicio Nacional de Geología y Minería, Carta Geológica de Chile, Serie Geología Básica, No. 83, Mapa Escala 1:100.000.

Liu, Ming, Yund, R.A., 1992. NaSi-CaAl interdiffusion in plagioclase. Am. Mineral. 77, 275–283.

Lohmar, S., 2008. Petrología de las ignimbritas Licán y Pucón (Volcán Villarrica) y Curacautín (Volcán Llaima) en los Andes del sur de Chile. (Ph.D. Thesis). Universidad de Chile, Chile.

Lohmar, S., Parada, M.-Á., Gutiérrez, F.J., Robin, C., Gerbe, M.C., 2012. Mineralogical and numerical approaches to establish the pre-eruptive conditions of the mafic Licán Ignimbrite, Villarrica Volcano (Chilean Southern Andes). J. Volcanol. Geotherm. Res. 235–236:55–69. https://doi.org/10.1016/j.jvolgeores.2012.05.006.

López-Escobar, L., Parada, M.-Á., Hickey-Vargas, R., Frey, F.A., Kempton, P.D., Moreno, H., 1995. Calbuco volcano and minor eruptive centers distributed along the Liquiñe-Ofqui Fault Zone, Chile (41°–42° S): contrasting origin of andesitic and basaltic magma in the Southern Volcanic Zone of the Andes. Contrib. Mineral. Petrol. 119: 345–361. https://doi.org/10.1007/BF00286934.

Martin, V.M., Morgan, D.J., Jerram, D.A., Caddick, M.J., Prior, D.J., Davidson, J.P., 2008. Bang! Month-scale eruption triggering at Santorini volcano. Science 321:1178. https://doi.org/10.1126/science.1159584.

McDonough, W.F., Sun, S.s., 1995. The composition of the Earth. Chem. Geol. 120: 223–253. https://doi.org/10.1016/0009-2541(94)00140-4.

McGee, L.E., Brahm, R., Rowe, M.C., Handley, H.K., Morgado, E., Lara, L.E., Turner, M.B., Vinet, N., Parada, M.-Á., Valdivia, P., 2017. A geochemical approach to distinguishing competing tectono-magmatic processes preserved in small eruptive centres. Contrib. Mineral. Petrol. 172. https://doi.org/10.1007/s00410-017-1360-2.

Millet, M.A., Tutt, C.M., Handler, M.R., Baker, J.A., 2014. Processes and time scales of dacite magma assembly and eruption at Tauhara volcano, Taupo Volcanic Zone, New Zealand. Geochem. Geophys. Geosyst. 15:213–237. https://doi.org/10.1002/2013GC005016.

Moreno, H., Lara, L.E., 2008. Geología del área Pucón-Curarrehue, regiones de La Araucania y De Los Ríos. Servicio Nacional de Geología y Minería, Carta Geológica de Chile, Serie Geológica Básica. No. 115, Mapa Escala 1:100.000.

Morgado, E., Parada, M.-Á., Contreras, C., Castruccio, A., Gutiérrez, F.J., McGee, L.E., 2015. Contrasting records from mantle to surface of Holocene lavas of two nearby arc volcanic complexes: Caburgua-Huelemolle Small Eruptive Centers and Villarrica Volcano, Southern Chile. J. Volcanol. Geotherm. Res. 306:1–16. https://doi.org/10.1016/j.jvolgeores.2015.09.023.

Morgan, D.J., Blake, S., Rogers, N.M., De Vivo, B., Rolandi, G., Davidson, J.P., 2006. Magma chamber recharge at Vesuvius in the century prior to the eruption of A.D. 79. Geology 34:845–848. https://doi.org/10.1130/G22604.1.

Müller, T., Dohmen, R., Becker, H.W., ter Heege, J.H., Chakraborty, S., 2013. Fe-Mg interdiffusion rates in clinopyroxene: experimental data and implications for Fe-Mg exchange geothermometers. Contrib. Mineral. Petrol. 166:1563–1576. https://doi.org/10.1007/s00410-013-0941-y.

O'Neill, H.S.C., Pownceby, M.I., 1993. Thermodynamic data from redox reactions at high temperatures. I. An experimental and theoretical assessment of the electrochemical method using stabilized zirconia electrolytes, with revised values for the Fe–"FeO", Co–CoO, Ni–NiO and Cu–Cu2O. Contrib. Mineral. Petrol. 114, 296–314.

Pavez, A., 1997. Geología e historia evolutiva del Complejo Volcánico Quetrupillán, Andes del Sur, 39.5° L.S. VIII Congreso Geológico Chileno, Actas. 2 pp. 1443–1447.

Pearce, T.H., 1968. A contribution to the theory of variation diagrams. Contrib. Mineral. Petrol. 19:142–157. https://doi.org/10.1007/BF00635485.

Petit-Breuilh, M.E., 1994. "Área volcánica Villarrica-Quetrupillán-Lanín" Marco general de su geografía histórica. Fondecyt Project 193-0992. Final Report.

Putirka, K.D., 2008. Thermometers and barometers for volcanic systems. Rev. Mineral. Geochem. 69:61–120. https://doi.org/10.2138/rmg.2008.69.3.

Ruprecht, P., Bachmann, O., 2010. Pre-eruptive reheating during magma mixing at Quizapu volcano and the implications for the explosiveness of silicic arc volcanoes. Geology 38:919–922. https://doi.org/10.1130/G31110.1.

Russell, J.K., Nicholls, J., 1988. Analysis of petrologic hypotheses with Pearce element ratios. Contrib. Mineral. Petrol. 99:25–35. https://doi.org/10.1007/BF00399362.

Sánchez, P., Pérez-Flores, P., Arancibia, G., Cembrano, J., Reich, M., 2013. Crustal deformation effects on the chemical evolution of geothermal systems: the intra-arc Liquiñe-Ofqui fault system, Southern Andes. Int. Geol. Rev. 55:1384–1400. https://doi.org/10.1080/00206814.2013.775731.

Sauerzapf, U., Lattard, D., Burchard, M., Engelmann, R., 2008. The titanomagnetite-ilmenite equilibrium: new experimental data and thermo-oxybarometric application to the crystallization of basic to intermediate rocks. J. Petrol. 49:1161–1185. https://doi.org/10.1093/petrology/egn021.

Stanley, C.R., Russell, J.K., 1989. Petrologic hypothesis testing with Pearce element ratio diagrams: derivation of diagram axes. Contrib. Mineral. Petrol. 103:78–89. https://doi.org/10.1007/BF00371366.

Streck, M.J., Broderick, C.A., Thornber, C.R., Clynne, M.A., Pallister, J.S., 2008. Plagioclase populations and zoning in dacite of the 2004–2005 Mount St. Helens eruption: constraints for magma origin and dynamics. US Geol. Surv. Prof. Pap. 34, 791–808.

Van Orman, J.A., Crispin, K.L., 2010. Diffusion in oxides. Rev. Mineral. Geochem. 72: 757–825. https://doi.org/10.2138/rmg.2010.72.17.

Waters, L.E., Lange, R.A., 2015. An updated calibration of the plagioclase-liquid hygrometer-thermometer applicable to basalts through rhyolites. Am. Mineral. 100: 2172–2184. https://doi.org/10.2138/am-2015-5232.

Wright, H.M.N., Folkes, C.B., Cas, R.A.F., Cashman, K.V., 2011. Heterogeneous pumice populations in the 2.08-Ma Cerro Galán Ignimbrite: implications for magma recharge and ascent preceding a large-volume silicic eruption. Bull. Volcanol. 73:1513–1533. https://doi.org/10.1007/s00445-011-0525-5.